Heliyon 10 (2024) e33612

Contents lists available at ScienceDirect

Heliyon

journal homepage: www.cell.com/heliyon

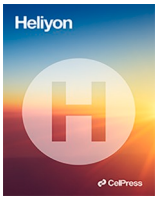

Research article

# Synthesizing Si/SiOC composites through different sol-gel reaction routes for lithium-ion battery anode materials

Bo-chen Huang, Li-yan Tsui, Settu Ramki, Hsiao-ping Hsu, Chung-wen Lan *

*Department of Chemical Engineering, National Taiwan University, Taipei, 106319, Taiwan*

ARTICLE INFO

*Keywords:*
Silane
Spherical SiOC
Bulk SiOC
Si/SiOC composite
Lithium-ion battery
Anode material

ABSTRACT

Silicon oxycarbide (SiOC) exhibits good retention and a reasonable specific capacity and is an alternative to silicon used as an anode material for high-performance lithium-ion batteries. However, SiOC generally shows a low Initial Coulombic Efficiency (ICE), wasting the lithium from the cathode. This work explores different sol-gel routes to synthesize SiOC from silanes and compares their performance. We found that the crushed bulk acid-catalyzed SiOC is simple and cost-effective but with excellent performance. Adding dimethyldimethoxysilane (DMDMS) by decreasing the oxygen content further enhances the battery performance. Building upon the excellent performance of SiOC, we further embed nano-silicon into SiOC. The Si/SiOC composites achieved a significantly higher specific capacity of 2185 $mAhg^{-1}$ and an impressive ICE of 77 % with acceptable battery retention.

## 1. Introduction

With the development of electric vehicles, the low energy density of conventional lithium-ion batteries (LIBs) has become a limitation, primarily due to graphite anodes' low theoretical specific capacity. Some research efforts have been made to enhance the performance of LIBs. For instance, Chen et al. developed ultrahigh separator porosity to achieve high-flux LIBs, providing excellent areal energy density for the full cell [1]. Additionally, Gautam et al. utilized rice husk to develop silicon-based anode materials, which possess both high theoretical capacity and environmental friendliness [2]. Furthermore, research on lithium-sulfur batteries is also thriving due to their considerable energy density. However, challenges such as volume expansion of lithium metal anodes and lithium dendrite growth still need to be addressed [3].

Silicon-based anodes have emerged as a promising material for LIBs and have been extensively studied. Compared to the current commercial graphite anodes with a theoretical specific capacity of 372 $mAhg^{-1}$ [4], silicon boasts an impressive theoretical specific capacity of up to 4200 $mAhg^{-1}$ [5]. However, the significant volume expansion (>300 %) during charge-discharge processes leads to continuous destruction of the solid-electrolyte interphase (SEI), causing rapid capacity decay and hindering commercial applications. To improve the cycle performance of silicon anodes, reducing silicon particles to nano size can help suppress structural damage caused by volume expansion, but it does not entirely prevent capacity fading [6]. Numerous studies have explored using carbon-coated nano-silicon to enhance its cycle performance. However, the results could have been much better. For instance, Tao et al. attempted to coat a carbon shell on silicon with polyvinylpyrrolidone (PVP). Still, the structure ultimately fractured, necessitating the addition of another layer of $SiO_2$ to improve the cycle performance [7].

* Corresponding author.
*E-mail address:* cwlan@ntu.edu.tw (C.-w. Lan).

https://doi.org/10.1016/j.heliyon.2024.e33612
Received 2 June 2024; Received in revised form 20 June 2024; Accepted 24 June 2024
Available online 25 June 2024

Silicon oxycarbide (SiOC), a derivative of silicon-based anodes, has been the subject of extensive research. The structure of SiOC consists of $SiO_xC_{4-x}$ tetrahedra surrounded by free carbon, creating a unique amorphous configuration that contributes to maintaining structural stability during charge and discharge [8], resulting in excellent cycle performance. However, SiOC needs higher initial Columbic efficiency (ICE) for commercial applications, but this remains a significant challenge [9].

A viable direction is Si/SiOC composites, combining silicon and SiOC as the anode materials. Choi et al. considered the carbon shell and SiOC coating separately for nano-silicon [10]. They introduced nano-silicon into phenyltrimethoxysilane (PTMS) vapor through ultrasonic spray and then pyrolyzed it. They found that the carbon shells on the carbon-coated samples suffered from breakage, leading to poor cycle performance. In contrast, silicon coated with SiOC demonstrated excellent cycle stability. Moreover, incorporating nano-silicon into SiOC enhances specific capacity and ICE. These give Si/SiOC a promising path in developing silicon-based anode materials.

Wu et al. synthesized Si/SiOC nanocomposites using phenyltrimethoxysilane (PTMS) as the SiOC precursor [11]. They formed emulsified droplets using the surfactant Triton x-100 and then underwent a sol-gel reaction in an alkaline environment to produce spherical products [11]. However, SiOC produced by phenylsiloxane is a thermoplastic polymer, causing the structure to deform during high-temperature pyrolysis and lose its spherical shape. The high carbon content also led to the problem of low specific capacity. Jiang et al. explored phosphorus doping in vinyltrimethoxysilane (VTMS) for sol-gel reaction [12]. After calcination, nano-particle phosphorus remained, forming P/SiOx/C composites. These composites needed to be ball-milled to an appropriate particle size to enhance their battery performance.

In these methods for preparing SiOC composites, we have noticed variations in the silicon precursors used. The differences in silane precursors impact the material's carbon content and structure stability after calcination. Morphology is also different based on the preparation method, with either spherical or bulk particles; ball milling is necessary if the particles are too large. A consistent comparison of various routes and morphologies for SiOC synthesis would be required. However, such a comparison has yet to be carried out so far. We first built upon our previous work by utilizing methyltrimethoxysilane (MTMS) as a silane precursor to synthesize SiOC. The advantage was its lower carbon content, higher material capacity, and maintaining inherent morphology after calcination. On the other hand, during synthesis, the solid content was low, and the emission cost was high. Different routes to generate spherical or bulk materials were considered, and both had a much higher solid content and much lower liquid emission. As a result, they have the potential for SiOC synthesis with improved battery performance at lower manufacturing costs. Ultimately, through the optimized process, silicon was further embedded into SiOC to form Si/SiOC composites to enhance battery performance further.

In the first method, we built upon our prior success with the Stöber-like reaction in synthesizing spherical SiOC [13]; we sought to further enhance its electrical characteristics by embedding silicon powder. To our knowledge, no one has previously explored the augmentation of battery performance by incorporating silicon powder into SiOC spheres using this method [8,14–16]. We were inspired by Demirörs et al. [17] to employ PVP for surface modification of nano-silicon and then utilize the sol-gel technique for nanoparticle coating.

The second approach was to emulsify silane into spherical droplets before sol-gel synthesis of spherical SiOC composites [11, 18–21]. The silicon nanoparticles were adjusted to be hydrophobic to stay in the silane phase. Moreover, substantial research has been dedicated to bulk SiOC composites [12,20,22,23]. We thus considered MTMS with an acid catalyst for bulk SiOC synthesis. The advantage was that the gel product had almost no morphology change after calcination and had a relatively low carbon content compared to phenyl- or vinyl-siloxane [11,21].

Previous studies have used various methods and different silicon precursors to produce Si/SiOC composites, making systematic comparisons difficult because they have yet to be carried out on the same platform. Therefore, this study comprehensively explores Si/SiOC composites from different synthesis routes; silicon content and diverse morphologies and their impact on battery performance are considered.

We have used MTMS as the fixed silicon precursor material in these three routes to compare their battery performance. We also tried to enhance SiOC's battery performance by adding dimethyldimethoxysilane (DMDMS) with a lower oxygen content. It is expected that a better route will be found to synthesize Si/SiOC composites that have better battery performance and are suitable for industrial production.

## 2. Experimental

### 2.1. Solution preparation

MTMS (95 %) and DMDMS (95 %) were purchased from Ya-Hu-Chi Industrial Co., Taiwan. 3-aminopropyltriethoxysilane (APS, 98 %) and ethanol (EtOH, 95 %) were purchased from Echo Chemical Co., Taiwan. Ammonium hydroxide ($NH_4OH$, 29 %) and hydrochloric acid (HCl, 36.5 %) were purchased from Re-New Chemical Material Co., Taiwan. All chemicals were used as received. AUO Co. supplied kerf-loss Si, and silicon nanosheets were obtained from Bluestar Materials Co.; silicon nanosheets were synthesized using an aluminum reduction method. The aluminum doping helped improve the electrical conductivity, resulting in a higher ICE, which will be discussed shortly. The size was around 3 μm with an average thickness of less than 100 nm. After ball milling, the width was about 200 nm, and the thickness remained the same.

The schematic of the material synthesis process is shown in Fig. A.1 and Fig. A.2, respectively.

**Raw Si/SiOC:** We followed our previous work using the Stöber-like method [13] to synthesize the material. The compositions of the initial solutions (precursor solution A) before pre-hydrolysis are shown in Table 1. The precursor solution A was hydrolyzed in a 40 °C water bath overnight. PVP-modified nano-silicon was added to solution A and fully dispersed by stirring and ultrasonication.

Solution B was an ammonia aqueous solution, and the concentration was adjusted by mixing 29 % ammonia solution with deionized water. The reaction started by mixing two solutions in a 30 °C water bath and finished after 2 h. The product was filtrated and dried in a 60 °C vacuum oven. The material was named Raw Si/SiOC$_{-x}$, where x means the molar ratio of Si/SiOC.

**Emulsion Si/SiOC:** We followed the work by Gong et al. as a reference [21]. The precursor solution is shown in Table 2. We first mixed nano-silicon and silane in the ethanol and DI water solvent with CTAB and then fully dispersed and emulsified by stirring and ultrasonication before adding the ammonia solution. After stirring for 5 min, we added the PVP solution. Reaction finished after 3 h. The product was collected by filter and dried in a 60 °C vacuum oven. The material was named Emulsion Si/SiOC$_{-x}$, x means the molar ratio of Si/SiOC.

**Bulk Si/SiOC:** The precursor solution is shown in Table 3. We mixed nano-silicon and silane and then entirely dispersed them by stirring and ultrasonication. We further used HCl as a reaction catalyst with some ethanol in a blender to get the bulk material with an irregular morphology. The crushing using the blender effectively got the sand-like product, and the setup was particularly suitable for scale-up. The product was filtrated and dried in a 60 °C vacuum oven. The material was named Bulk Si/SiOC-DM$_{x-y}$, where x means the ratio of DMDMS/MTMS and y represents the molar ratio of Si/SiOC. In this method, we used DMDMS as one of the precursors to decrease oxygen content and use APS as a co-condensation catalyst [24].

**SiOC:** For comparison, we also synthesize **Raw SiOC**, **Emulsion SiOC,** and **Bulk SiOC-DM$_x$** according to the previous procedures but without adding nano-silicon.

### 2.2. Calcination and ball milling

The dried product was placed in an alumina crucible for calcination in a tube furnace. The furnace temperature was increased to 1100 °C at a heating rate of 5 °Cmin$^{-1}$ and maintained for 3 h in an argon atmosphere before cooling. Bulk SiOC and Bulk Si/SiOC would be milled for 30 min at 350 rpm by a 5 mm steel ball using a planetary ball mill (FRITSCH, Pulverisette). The morphology is shown in Fig. A4g.

### 2.3. Material characterizations

The morphologies of the Si/SiOC composites were examined by a field emission scanning electron microscope (FE-SEM, NOVA NanoSEM 230) with a 5–8 kV accelerating voltage. The Bulk Si/SiOC specimen was first prepared by a dual-beam focused ion beam (FIB, FEI Quanta 3D FEG) and further imaged by transmission electron microscopy (TEM, FEI Tecnai G2 F-20 S-TWIN). The size distribution of Raw Si/SiOC was analyzed using the software ImageJ. The size distribution of Bulk Si/SiOC was analyzed with Zetasizer Nano ZS (Malvern Instrument). Raman spectra were collected on a micro-Raman spectrometer (Horiba, iHR550). The elemental compositions of the particle surface and the X-ray photoelectron spectra were conducted using X-ray photoelectron spectroscopy (XPS, Thermo Scientific Nexsa G2 Surface Analysis System, Theta Probe). An X-ray beam (Al Kα X-ray source, 1486.68eV) of 400 μm size was used. The spectra were acquired in the constant analyzer energy mode with pass energy of 50eV. Charge compensation was achieved with the system dual beam flood gun. The Thermo Scientific Avantage software, version 6.5.1 was used for data collection and processing. The oxygen and carbon contents of the whole particles were determined by an oxygen-nitrogen analyzer (HORIBA, EMGA-820) and a carbon-sulfur analyzer (HORIBA, EMIA-320V2), respectively.

### 2.4. Electrochemical measurements

Electrodes were made by mixing the active material, carboxymethyl cellulose (CMC), carbon black, and styrene-butadiene rubber (SBR) in the mass ratio of 70:11.25:15:3.75 with deionized water, and then the slurry was spread onto a copper foil. After the electrodes were dried at 80 °C under vacuum overnight, CR2032 coin-type half cells were assembled in a glove box. The mass loading of the active materials on the electrode was 0.88 ± 0.14 mg cm$^{-2}$ 1 M $LiPF_6$ in a mixture of dimethyl carbonate (DMC): ethylene carbonate (EC): propylene carbonate (PC): ethyl-methyl carbonate (EMC) = 30:25:10:20 by weight with 10 wt% fluoroethylene carbonate (FEC) addition served as the electrolyte. The galvanostatic measurements were carried out in the potential range of 0.005 V to 2V, and the current density was 0.1 Ag$^{-1}$ for the first cycle, 1 Ag$^{-1}$ for 2–10 cycles, and 2 Ag$^{-1}$ for subsequent cycles by a cell test instrument (NEWARE ABT-408T 5V50mA-164-U). The cyclic voltammetric (CV) measurement (CH Instruments 1211C) was scanned at 0.1 mVs$^{-1}$ in the voltage region of 0.005 V–2 V for the initial three cycles.

**Table 1**
Composition of precursor solution A for Raw SiOC.

| | MTMS | EtOH | $H_2O$ | HCl |
|---|---|---|---|---|
| 0.11 M MTMS | 3.28 mL | 169.47 mL | 43.62 mL | 0.0012 mL |

**Table 2**
Composition of precursor solution for Emulsion SiOC.

| | MTMS | EtOH | $H_2O$ | CTAB | $NH_4OH$ | PVP |
|---|---|---|---|---|---|---|
| Emulsion | 0.47 mL | 16.54 mL | 25.30 mL | 0.08 g | 0.51 mL | 0.025 g |

**Table 3**
Composition of precursor solution for Bulk SiOC.

| | MTMS | DMDMS | APS | 1 M HCl |
|---|---|---|---|---|
| DM0 | 5 mL | 0 mL | 0 mL | 5 mL |
| DM0.5 + 5%APS | 3.33 mL | 1.67 mL | 0.247 mL | 5 mL |
| DM0.5 + 15%APS | 3.33 mL | 1.67 mL | 0.742 mL | 5 mL |

## 3. Results and discussion

### 3.1. Raw Si/SiOC synthesized by Stöber-like method

We used the Stöber-like method to make SiOC beads [13]. This reaction method required strict control of conditions, including temperature, time, concentration of reactants, and alkaline catalyst. The process required a significant amount of solution with low solid content, but it could produce monodisperse SiOC beads of different sizes through concentration control.

We first embedded ball-milled kerf-loss Si into the SiOC beads. Fig. 1a shows the SEM image of the silicon morphology; the particle size is about 50–200 nm. Fig. 1b shows the morphology of SiOC beads, about 1 μm in size. The embedding, as shown in Fig. 1c, was not successful. However, if we modified the silicon surface using PVP, inspired by Demirörs et al. [17], the sol-gel reacted uniformly on the silicon surface. As shown in Fig. 1d–f, the results reveal successful silicon encapsulation within the SiOC beads. However, there was a significant aggregation of particles. We tried to decrease solid content by decreasing silane concentration to prevent aggregation. According to our previous work, SiOC beads with different particle sizes can be synthesized using different silane concentrations [13]. We used 0.11 M MTMS to synthesize about 200 nm SiOC beads (Fig. 2a). With varying ratios of Si/PVP (Fig. 2b–e), we found Si/PVP = 5 was suitable for monodispersed Si/SiOC composite beads.

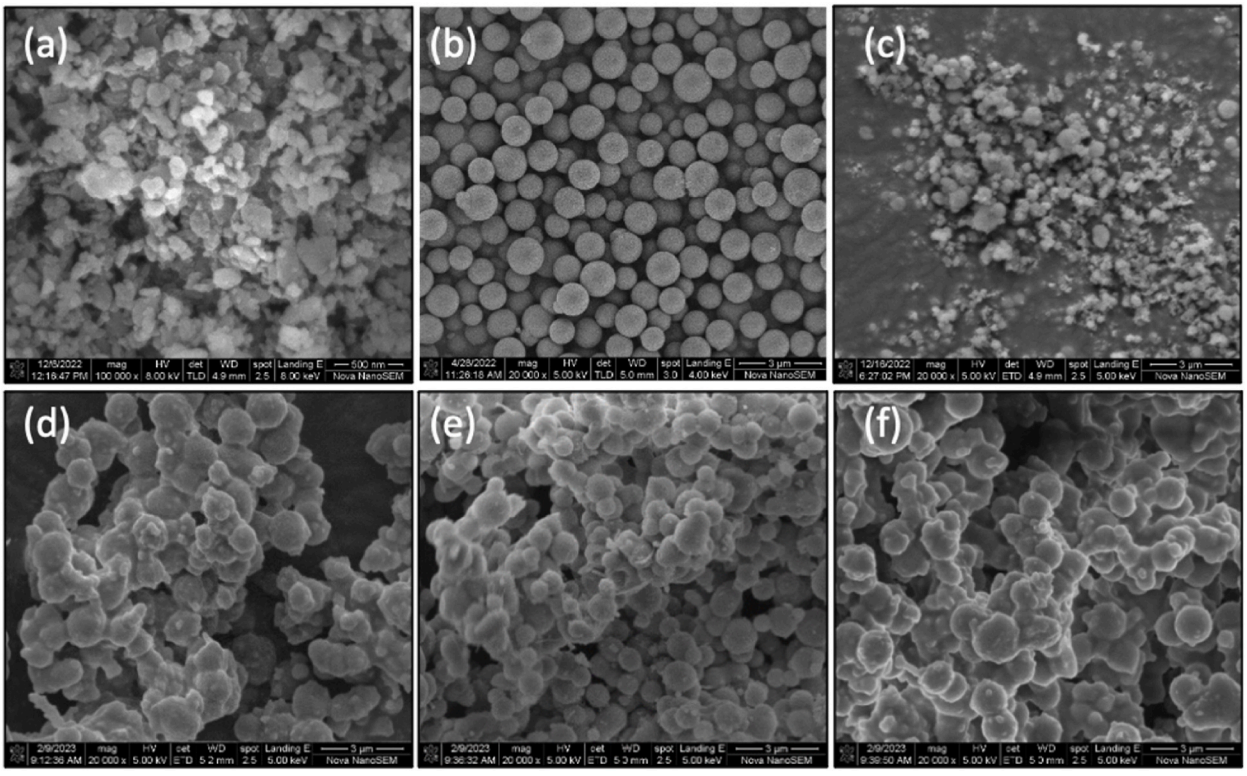


**Fig. 1.** SEM images of Raw Si/SiOC composites: (a) Kerf-loss Si, (b) Raw SiOC; 0.59 M MTMS+4.4 M $NH_4OH$, (c)–(f) Si embedded in SiOC; Si/SiOC = 1; Si+0.59 M MTMS+4.4 M $NH_4OH$, (c) Si without PVP wash, (d) Si/PVP = 0.25, (e) Si/PVP = 1, (f) Si/PVP = 5.

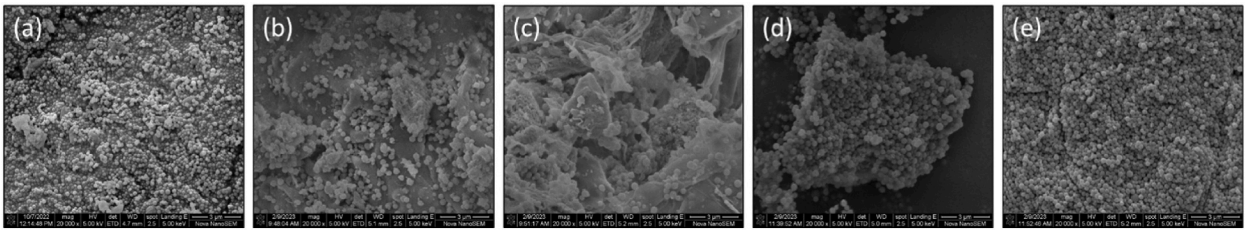


**Fig. 2.** SEM images of Raw Si/SiOC composites: (a) Raw SiOC; 0.11 M MTMS+0.73 M $NH_4OH$, (b)–(e) Si embedded in SiOC; Si/SiOC = 1; Si+0.11 M MTMS+0.73 M $NH_4OH$, (b) Si/PVP = 0.25, (c) Si/PVP = 0.5, (d) Si/PVP = 1, (e) Si/PVP = 5.

Because nano-silicon (from Bluestar Materials Co.) had a higher ICE in the half-cell performance due to the improved electrical conductivity by Al doping (Fig. A5), we also embedded them into SiOC as Raw Si/SiOC composites. Figure A6a shows the excellent morphology of Raw Si/SiOC composites. The particle size of composites was slightly higher than Raw SiOC, indicating Si was embedded in the beads (Fig. A7). We also tried to increase the ratio of nano-silicon; however, the morphology became worse (Fig. A6b-c), which meant a limited amount of Si could be embedded.

### 3.2. Emulsion Si/SiOC

Preparing Si/SiOC spherical composites in a Stöber-like reaction required stringent control. Otherwise, it could lead to particle aggregation or reduced yields, rendering solvent recycling challenging and significant solvent wastage due to low solid content of only 0.4 %. An alternative method for synthesizing SiOC beads involves emulsifying silane before reaction, transforming it into oil-phase droplets dispersed in a water-phase medium. This process necessitates using surfactants to mix the water and oil phases uniformly. We adopted the work by Gong et al. using Cetyltrimethylammonium bromide (CTAB) as a surfactant for silane emulsification [21]. However, we employed MTMS as the silane precursor. As depicted in Fig. 3, using this approach, we successfully synthesized SiOC beads and Si/SiOC composites of approximately 600 nm particle size. The particle size and distribution were similar to Gong et al.'s work [21]. Due to the precursor's lower carbon content, our specific capacity could be expected to be higher. The advantage of this synthesis method was that the catalyst was only needed to ensure the continuous progression of the sol-gel reaction in the oil phase until completion. As a result, solvent recycling becomes feasible, making it suitable for industrial production.

### 3.3. Bulk Si/SiOC

The methods above for preparing SiOC involved using alkaline catalysis or emulsion to produce spherical products. We also attempted to synthesize SiOC bulk materials with irregular morphology to compare the battery performance. We adopted the approach by Jiang et al. [12]. They used acid-catalyzed condensation of VTMS to produce bulk P/SiOx/C composites. Compared to Jiang et al.'s work [12], we used MTMS as the precursor and adjusted the HCl concentration for appropriate condensation. The reactivity of MTMS and VTMS might be different in the acid environment. Moreover, we put everything with some ethanol in a blender for mixing and crushing to get the sand-like bulk Si/SiOC. Using a blender to agitate the reaction enhanced the composite's uniformity and crushed bulk particles, making it easier to mill large quantities of the product further. The reaction proceeded rapidly without the need for pre-hydrolysis of silane. Subsequent calcination of the sand-like material yielded black bulk SiOC. Before its utilization as anode material, ball milling was still required to decrease particle size to around 5 μm. Fig. 4 shows the SEM image and particle size distribution of Bulk SiOC and Si/SiOC composites.

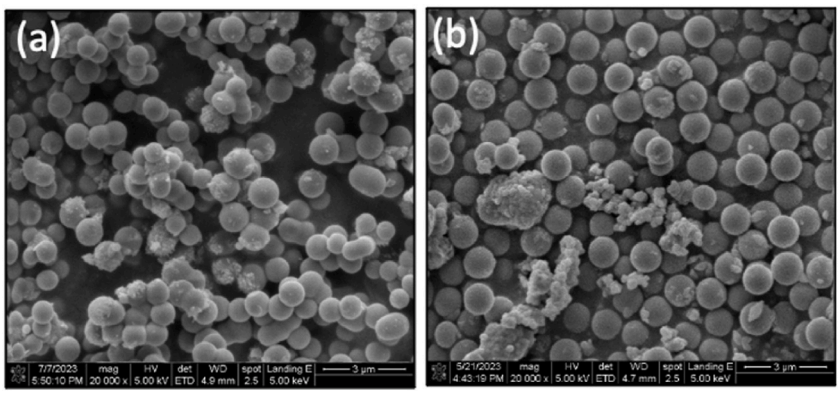


**Fig. 3.** SEM images of Emulsion Si/SiOC composites: (a) Emulsion SiOC and (b) Emulsion Si/SiOC-1.

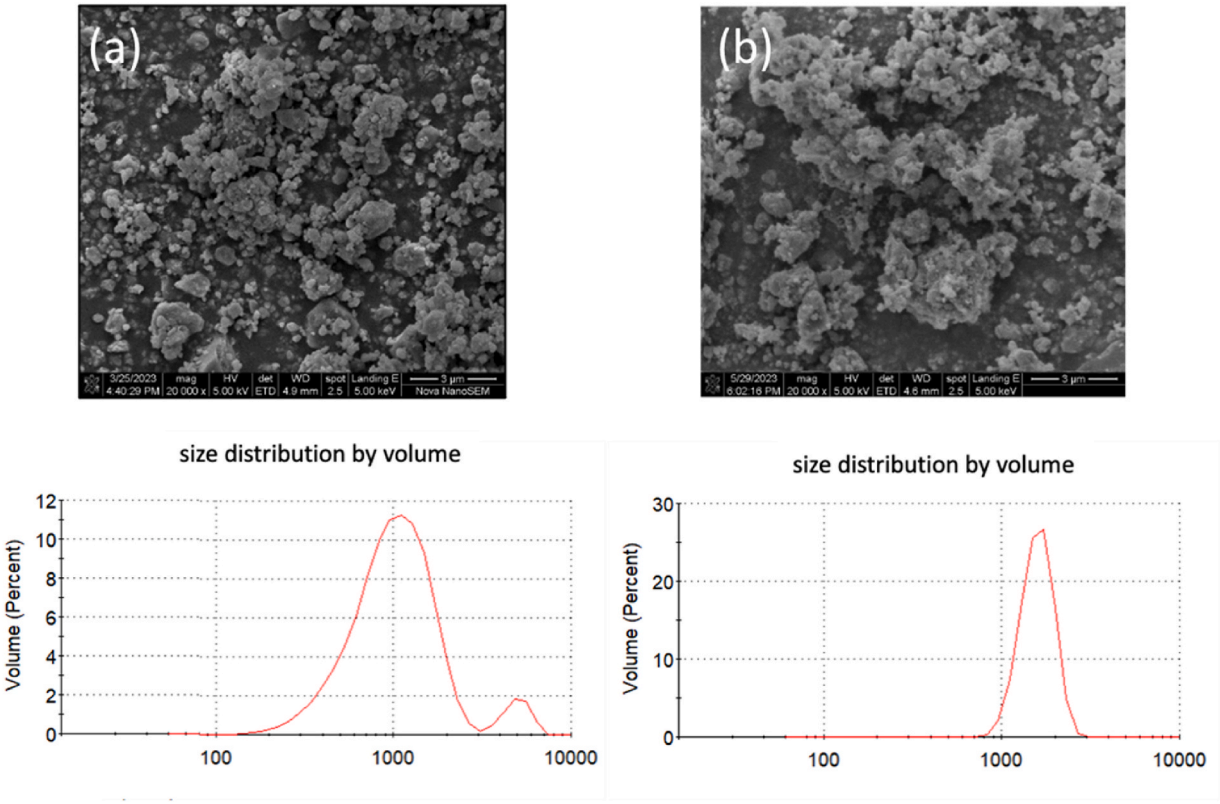


**Fig. 4.** SEM images and particle size distribution of Bulk SiOC and Si/SiOC composites: (a) Bulk SiOC-DM0 and (b) Bulk Si/SiOC-DM0-1.

We could check the distribution of Si by TEM image (Fig. A8). Selected area diffraction patterns (SADPs) show the presence of Si (111), Si (220), and Si (331). The dark field image shows the distribution of Si in amorphous SiOC. Bright regions correspond to signals of silicon crystallization, while dark regions represent amorphous SiOC or amorphous silicon.

### *3.4. Adding DMDMS*

To enhance battery performance, especially the ICE, the decrease of oxygen content is crucial for increasing ICE because it induces irreversible compounds like $Li_2O$ and lithium silicates in the first discharge [25,26]. We attempted to use DMDMS with a lower oxygen content as a precursor for SiOC. However, since a DMDMS molecule contains only two methoxy groups, its condensation cannot form a three-dimensional structure. Besides, DMDMS has high hydrophobicity, making it difficult to disperse in aqueous solvents and make a slurry. As a result, it needs to undergo co-condensation with MTMS. Referring to our previous work, we employed APS to facilitate MTMS and DMDMS co-condensation, successfully synthesizing Bulk SiOC with lower oxygen content. Compared to the synthesis of spherical SiOC, the reactivity in the Bulk SiOC process is higher, leading to a noticeable reduction in oxygen content. The comparison of elemental analysis is shown in Table 4. The spherical Raw SiOC and Bulk SiOC-DM0 are derived from MTMS as a precursor, so their oxygen content remains unchanged. When comparing different DM ratios, the oxygen content significantly decreased for DM0.5, while DM1 was similar to DM0.5, indicating that DM0.5 had reached the limit of the co-condensation reaction.

Fig. 5 and A.9 show the XPS spectra of SiOC-DM0 and DM0.5 calcined at 1100 °C for 3 h in the Ar atmosphere, respectively. The samples were etched for 60 s and 1200 s by an Argon ion beam at 500 V with 1 mA $cm^{-2}$. The C–C bond in C1s represents the presence of free carbon, while C–*O*–C and C═O may indicate surface oxidation caused by ball milling. The $SiO_3C$ and $SiO_2C_2$ bonds in O1s and

**Table 4**
Elemental composition of SiOC synthesized from different DMDMS/MTMS ratios after 1100 °C 3 h Ar calcination measured by oxygen-nitrogen and carbon-sulfur analyzers.

| | C wt% | O wt% | Formula |
|---|---|---|---|
| Raw SiOC | 12.05 % | 37.40 % | $SiO_{1.30}C_{0.35}+C_{0.21}$ |
| Bulk SiOC-DM0 | 11.24 % | 37.72 % | $SiO_{1.30}C_{0.35}+C_{0.16}$ |
| Bulk SiOC-DM0.5 | 14.01 % | 32.34 % | $SiO_{1.06}C_{0.47}+C_{0.14}$ |
| Bulk SiOC-DM1 | 14.76 % | 32.73 % | $SiO_{1.09}C_{0.46}+C_{0.20}$ |

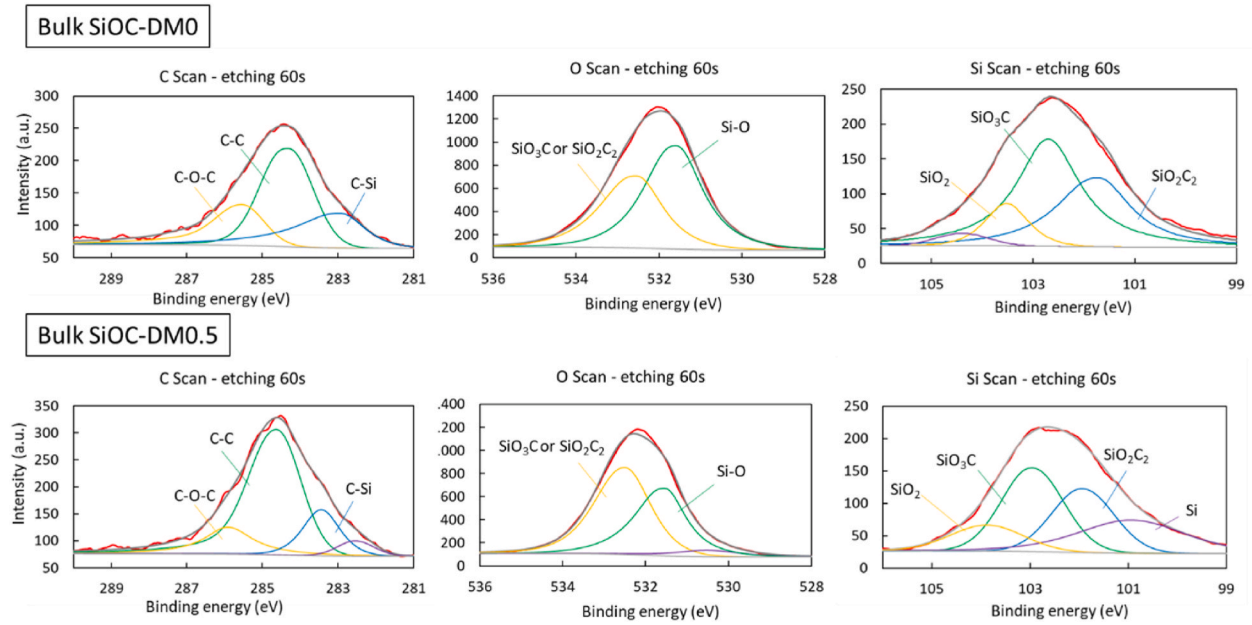


**Fig. 5.** Si2p, C1s, and O1s XPS spectra of SiOC (60 s etching).

Si2p represent the presence of bonded carbon. The Si2p spectrum shows the composition of Si–*O*–C bonds. In the spectrum of the 60-s etch, the presence of the O═C–N- bond in DM0.5 indicates the involvement of the co-condensing agent APS in the bonding, introducing nitrogen-doped effects that may enhance material conductivity. This is only detected in the 60-s etch signal, suggesting a low concentration. From the 60 s and 1200 s etching, the remaining composition differences between near-surface and inner are minimal, with slight variations in carbon, oxygen, and silicon content distribution. Table 5 shows the elemental analysis of DM0 and DM0.5 at different etch times. The inner layers have lower oxygen content, indicating an increase in silicon-carbon bonds and a higher distribution of free carbon on the surface. Comparing DM0 and DM0.5, the latter exhibits significantly lower oxygen content and higher carbon content, which contributes to improved material ICE.

### 3.5. Raman analysis

Figure A.10 shows the Raman analysis results of different SiOC samples. Strong D and G bands are present in all spectrums, which are characteristics of carbon materials. The D band (1350 $cm^{-1}$) represents disordered vibrations induced by aromatic ring structures, with its intensity correlated to amounts of aromatic rings. The G band (1580 $cm^{-1}$) originates from stretching vibrations of sp2 hybridized carbon atoms within aromatic rings or chain structures [27].

Based on the spectroscopic results, the ID/IG ratios were calculated (Table A1). Bulk SiOC-DM0.5 and Emulsion SiOC exhibit relatively high ID/IG ratios, indicating a higher presence of disordered carbon as evidenced by the more intense D bands [19]. It is speculated that due to the presence of two methyl groups in DMDMS that do not participate in the condensation reactions, more amorphous carbon is generated after pyrolysis. For Emulsion SiOC, introducing CTAB as a surfactant to emulsified silane and adding PVP to provide surface charge, preventing particle aggregation, could cause additional carbon during pyrolysis. This suggests that the increased amorphous carbon leads to more defects, resulting in higher ID/IG ratios in the material.

### 3.6. Electrochemical performance

Fig. 6 compares the battery performance of SiOCs. Firstly, Fig. 6a presents a comparison of specific capacity and ICE. The specific

**Table 5**
Elemental composition of SiOC measured by XPS.

| Etching time | Condition | C wt% | O wt% | Formula |
|---|---|---|---|---|
| 0 s | Bulk SiOC-DM0 | 17.90 % | 45.34 % | $SiO_{2.17}+C_{1.14}$ |
| | Bulk SiOC-DM0.5 | 22.00 % | 40.59 % | $SiO_{1.90}C_{0.05}+C_{1.33}$ |
| 60 s | Bulk SiOC-DM0 | 14.26 % | 42.54 % | $SiO_{1.73}C_{0.14}+C_{0.63}$ |
| | Bulk SiOC-DM0.5 | 23.19 % | 36.33 % | $SiO_{1.58}C_{0.21}+C_{1.13}$ |
| 1200 s | Bulk SiOC-DM0 | 13.68 % | 37.79 % | $SiO_{1.37}C_{0.32}+C_{0.34}$ |
| | Bulk SiOC-DM0.5 | 17.95 % | 32.78 % | $SiO_{1.17}C_{0.42}+C_{0.41}$ |

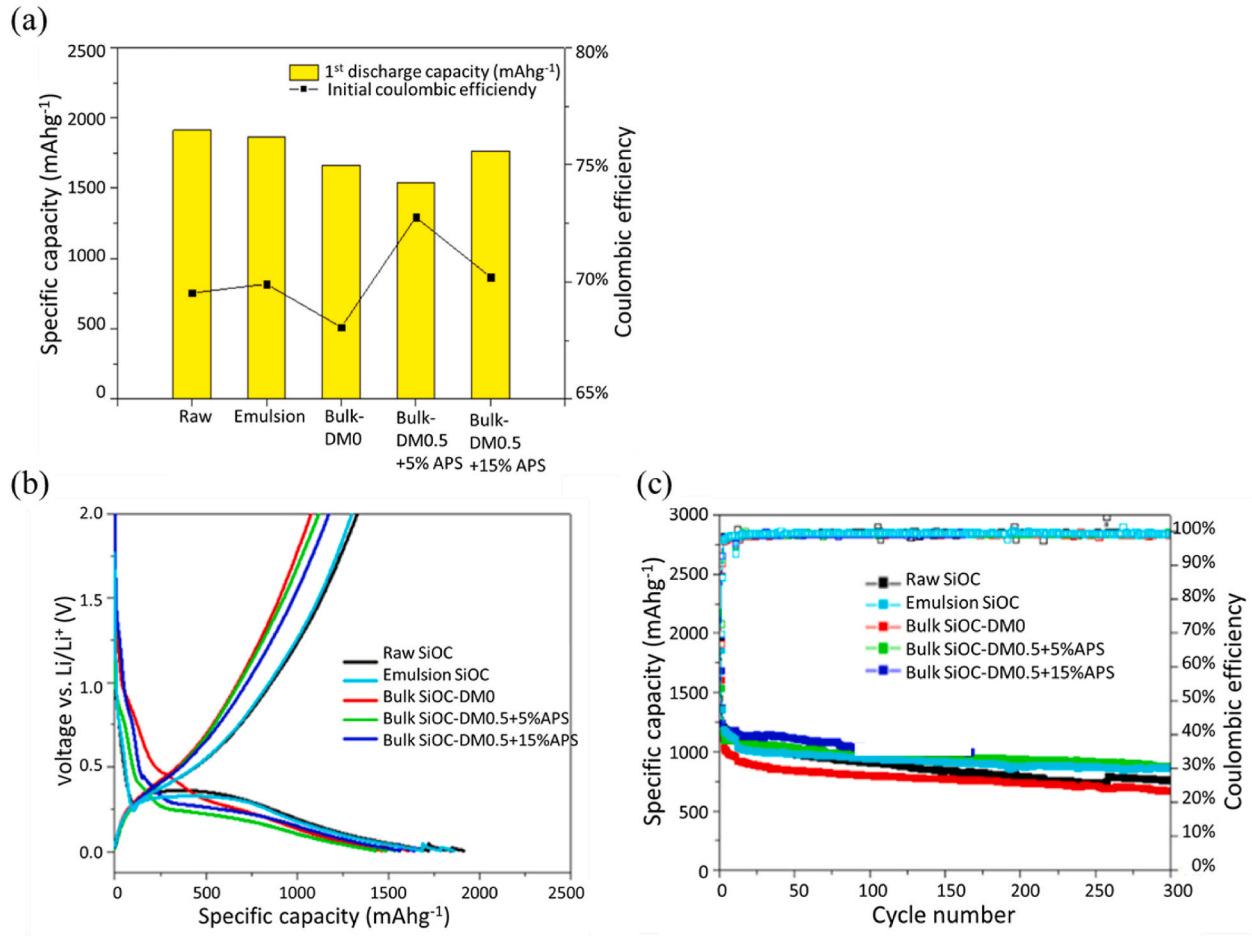


**Fig. 6.** (a) 1st discharge capacity and ICE of SiOC at a current density of 0.1 $Ag^{-1}$, (b) 1st charge/discharge curves of SiOC at a current density of 0.1 $Ag^{-1}$, and (c) Cycle performance and CE of SiOC.

capacity and ICE are similar when comparing the two types of SiOC beads. However, the ICE of Bulk SiOC-DM0 is comparatively lower. Nevertheless, the addition of DMDMS in DM0.5 shows improvement, with the material doped with 5 % APS achieving the highest ICE of 72 %.

For the retention performance (Fig. 6c), Emulsion SiOC exhibited better cycling capability in terms of spherical particles. Compared with Bulk SiOC, the cycling of Bulk SiOC-DM0 dropped faster in the initial 10 cycles but stabilized later. Due to its loose stack, we speculate that the bulk structure led to unstable lithium-ion transportation during cycling. On the other hand, the stack of spherical particles was denser, and the material's structure became more stable after expansion during cycling, resulting in lower irreversible capacity in subsequent cycles.

The incorporation of DMDMS in Bulk SiOC, DM0.5, improved ICE and stability during the early cycles, possibly due to the lower oxygen content and higher carbon amount, which enhanced conductivity and lithium-ion transport. Therefore, the cycle performance was improved. In conclusion, Emulsion SiOC and Bulk SiOC-DM0.5 are better SiOC materials, with 70 % and 86 % retention, respectively, after 150 cycles.

Figure A.12 compares Bulk Si/SiOC-$DM_0$ battery performance with varying embedded silicon contents. The specific capacity and ICE increased with the rise in silicon content. The specific capacity of Bulk Si/SiOC-0.33 and 0.67 shows a relatively low increase. Bulk Si/SiOC-1 demonstrated a significant rise in specific capacity and ICE, while during the cycle, the specific capacity experienced a gradual decline. When the Bulk Si/SiOC ratio reached as high as 1.4, the decline in specific capacity became remarkably pronounced.

Fig. 7 compares Raw Si/SiOC-1, Bulk Si/SiOC-DM0.5-1+15 % APS, and Emulsion Si/SiOC-1. All three embedding Si methods significantly enhanced the specific capacity and ICE. As for the cycle performance, the capacity decay of the bulk product was slower, indicating that the bulk particle provided better buffering for the expansion of embedded Si. After 150 cycles, it retained a specific capacity of 932 $mAhg^{-1}$ with a retention of 55 %.

In Table A2, we compare the electrochemical performance of our Bulk SiOC-DM0.5 + 15 % APS and Bulk Si/SiOC-DM0.5-1+15 % APS, with various SiOC anode material prepared by multiple literature that adopt similar process and characteristics. According to the reported data, our SiOC anode material has higher ICE in a lower charging range (0.005V–2V) and exhibited stable cycling

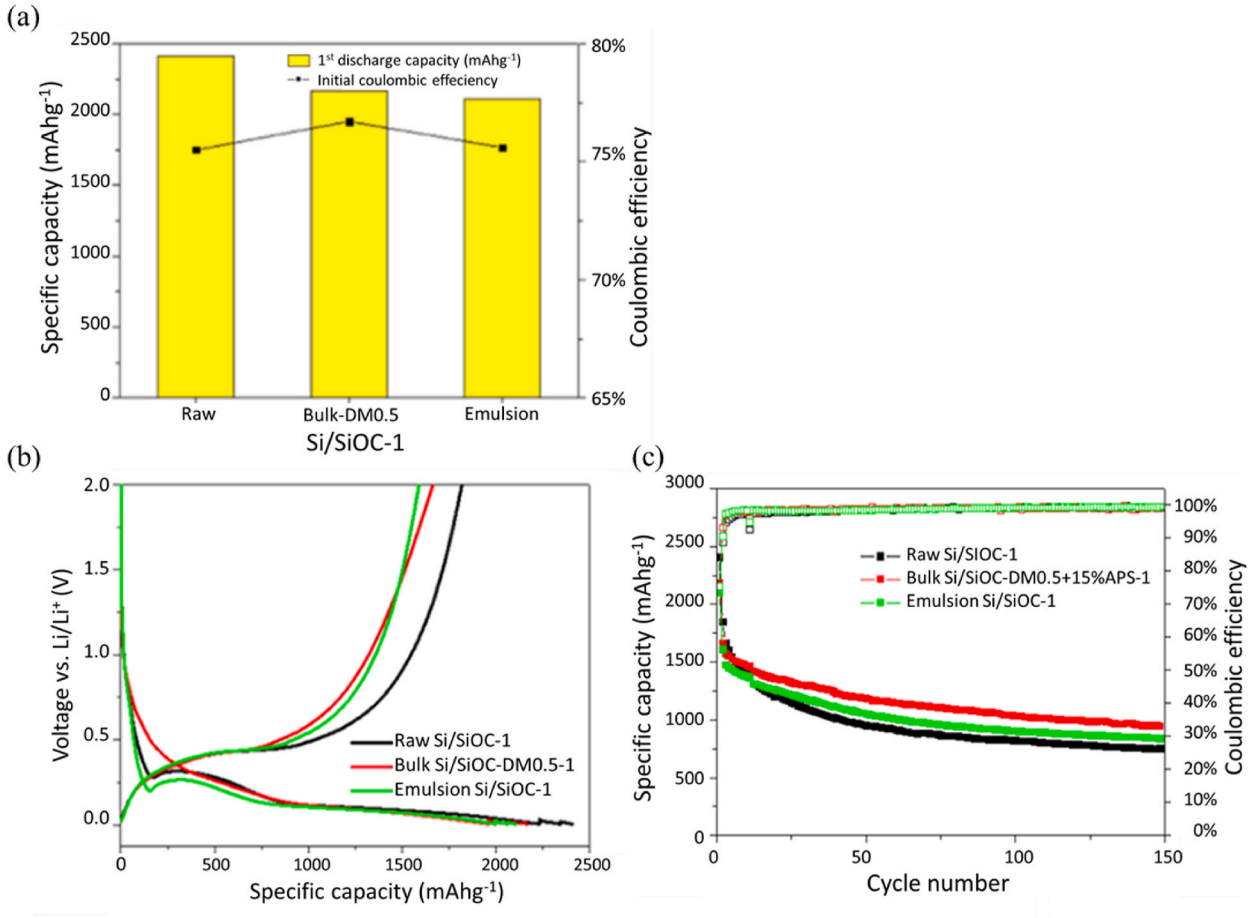


**Fig. 7.** (a) 1st discharge capacity and ICE of Si/SiOC at a current density of 0.1 $Ag^{-1}$, (b) 1st charge/discharge curves of Si/SiOC at a current density of 0.1 $Ag^{-1}$, and (c) Cycle performance and CE of Si/SiOC.

performance at higher current densities compared to many other compound presented in previous literatures. This is expected to arise from the aforementioned modification of carbon and oxygen species concentrations by our choice of silane precursors and suitable process, especially in our bulk products. The combination of one silane that possesses lower carbon with another owning lower oxygen compared to other widely used precursors, can mitigate the negative effect that these two elements has towards SiOC, while still being able to utilize the benefits too.

Moreover, with the fabrication of Si/SiOC composites we can further enhance the specific capacity and ICE. If a better silicon material were to be used to prepare bulk composites, it would have a better cycle performance.

Fig. 8 depicts the CV (cyclic voltammetry) curves of the first three cycles of Bulk SiOC and Bulk Si/SiOC anodes. Upon examining the SiOC portion, the oxidation peak at 0.52 V is attributed to the dealloying process of $Li_xSi$ [11]. The weak reduction peaks at 0.4 V and 0.7 V are associated with forming the solid electrolyte interphase (SEI) [28]. In contrast, the reduction peak at 1.4 V corresponds to irreversible reactions between the electrolyte and the electrode [15]. The irreversible lithium storage of $SiO_x$ near oxygen is observed between 0.01 V and 0.4 V.

Moving on to the Si/SiOC section, the oxidation peak at 0.33 V is attributed to the interaction between $Li^+$ and the Si–O network within SiOC. The peak at 0.52 V is related to the dealloying process of $Li_xSi$ [11]. These two peaks above and the reduction peak at 0.19 V significantly intensify after the first cycle. This indicates that the active material reacts more with Li, enhancing the electronic kinetics process [29].

Figure A.13 illustrates the rate capability of SiOC composites. Raw SiOC and Bulk SiOC-DM0 exhibited a decrease in specific capacity at high current densities, and the capacity did not fully recover upon returning to 0.1 $Ag^{-1}$. Their performance could be more favorable at high current densities. On the other hand, DM0.5 showed excellent performance, with almost no decrease in specific capacity at 3 $Ag^{-1}$. Both materials could recover their original capacity values upon returning to 0.1 $Ag^{-1}$.

Bulk Si/SiOC-DM0.5-1 also maintained high-rate performance, significantly increasing specific capacity at various current densities through embedding silicon.

Figure A.14 shows the morphology of Bulk SiOC electrodes before and after cycles. The appearance of bulk particles can be observed. From the post-cycling appearance, it could be seen that particles could still densely stack after experiencing expansion and

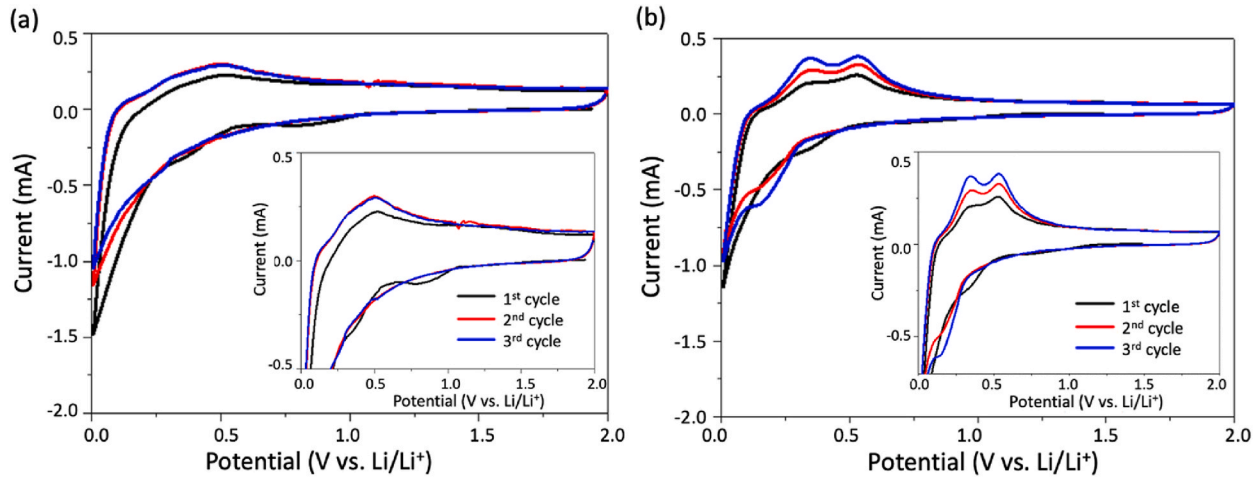


**Fig. 8.** Cyclic voltammetry curves of SiOC and Bulk Si/SiOC-DM0.5-1 at a scanning rate of 0.1 $mVs^{-1}$, and voltage range between 0.005 V and 2 V vs. $Li^{+}$/Li for the first 3 cycles: (a) Bulk SiOC-DM0.5 and (b) Bulk Si/SiOC-DM0.5-1.

contraction without many cracks. The retention for 432 cycles was 47 %, and the measured thickness increased by only 34 %. Therefore, good cycling performance could be achieved.

Figure A.15 shows the morphology of Bulk Si/SiOC electrodes before and after cycles. The electrodes appeared to be similar to Bulk SiOC before the cycles. However, after cycles, numerous surface protrusions are visible. It is speculated that the expansion of Si was significant, but it was wrapped without immediate cracking, resulting in these protrusions. Nevertheless, this caused gradual detachment of the electrode's active material, leading to a decline in cycle performance. The retention for 199 cycles was 48 %, and the measured thickness increased by 126 %.

## 4. Conclusions

This study compared different synthesis routes for preparing SiOC and Si/SiOC composites. The high reactivity of the acid-catalyzed sol-gel reaction for bulk SiOC was advantageous for incorporating DMDMS of low oxygen content as a silane precursor to enhance battery performance. This method has low production costs due to the use of a small amount of solvent and the affordability of silane. We also introduced a blender to address the issue of large bulk products that a stirrer could not effectively employ. The crushed products also facilitate large-scale ball milling production, and the ball milling production process is a mature technology in the industry, making it suitable for mass production.

Bulk SiOC-DM0.5, synthesized by an acid-catalyzed sol-gel process incorporating DMDMS, had the best battery performance in this study. The specific capacity of the material was over 1539 $mAhg^{-1}$, with an ICE of 72 % in the potential range of 0.005 V–2 V, and the capacity retention after 150 cycles was 86 % at a charging rate of $2Ag^{-1}$. This was among the best-reported data for the SiOC from DMDMS/MTMS.

To improve ICE, silicon was embedded to form Si/SiOC composites. Bulk Si/SiOC-DM0.5-1 obtained an ICE of 77 % in the potential range of 0.005 V–2 V. Regarding cycling performance, the capacity retention rates at 150 cycles were 55 %. If a better nano-silicon is used, the retention could be further improved.

## Data availability statement

Data will be made available on reasonable request to corresponding author:

## CRediT authorship contribution statement

**Bo-chen Huang:** Data curation, Conceptualization, Investigation, Methodology, Project administration, Resources, Visualization, Writing – original draft, Writing – review & editing. **Li-yan Tsui:** Investigation, Validation, Visualization, Writing – review & editing. **Settu Ramki:** Investigation, Validation. **Hsiao-ping Hsu:** Formal analysis, Investigation, Resources. **Chung-wen Lan:** Supervision.

## Declaration of competing interest

The authors declare the following financial interests/personal relationships which may be considered as potential competing interests: Chung-wen Lan reports financial support was provided by National Taiwan University. Chung-wen Lan reports a relationship with National Taiwan University that includes: employment. If there are other authors, they declare that they have no known competing financial interests or personal relationships that could have appeared to influence the work reported in this paper.

## Acknowledgments

This work was supported by the National Science and Technology Council of Taiwan and Nan Ya Plastics Co.

## Appendix A. Supplementary data

Supplementary data to this article can be found online at https://doi.org/10.1016/j.heliyon.2024.e33612.

## References

[1] D. Chen, Y. Liu, C. Feng, Y. He, S. Zhou, B. Yuan, W. He, Unified throughout-pore microstructure enables ultrahigh separator porosity for robust high-flux lithium batteries, Electron 1 (2023) e1, https://doi.org/10.1002/elt2.1.
[2] M. Gautam, G.K. Mishra, M. Furquan, K. Bhawana, D. Kumar, S. Mitra, Design of low-stress robust silicon and silicon-carbide anode with high areal capacity and high energy density for next-generation lithium-ion batteries, Chem. Eng. J. 472 (2023) 144916, https://doi.org/10.1016/j.cej.2023.144916.
[3] B. Song, L. Su, X. Liu, W. Gao, T. Wang, Y. Ma, Y. Wu, An examination and prospect of stabilizing Li metal anode in lithium–sulfur batteries: a review of latest progress, Electron 1 (2023) e13, https://doi.org/10.1002/elt2.13.
[4] J. Asenbauer, T. Eisenmann, M. Kuenzel, A. Kazzazi, Z. Chen, D. Bresser, The success story of graphite as a lithium-ion anode material-fundamentals, remaining challenges, and recent developments including silicon (oxide) composites, Sustain. Energy Fuels 4 (2020) 5387–5416, https://doi.org/10.1039/d0se00175a.
[5] H.K. Liu, Z.P. Guo, J.Z. Wang, K. Konstantinov, Si-based anode materials for lithium rechargeable batteries, J. Mater. Chem. 20 (2010) 10055–10057, https://doi.org/10.1039/c0jm01702g.
[6] U. Kasavajjula, C. Wang, A.J. Appleby, Nano- and bulk-silicon-based insertion anodes for lithium-ion secondary cells, J. Power Sources 163 (2007) 1003–1039, https://doi.org/10.1016/j.jpowsour.2006.09.084.
[7] T. Yang, X. Tian, X. Li, K. Wang, Z. Liu, Q. Guo, Y. Song, Double core–shell Si@C@SiO2 for anode material of lithium-ion batteries with excellent cycling stability, Chem. Eur J. 23 (2017) 2165–2170, https://doi.org/10.1002/chem.201604918.
[8] B. Krüner, C. Odenwald, N. Jäckel, A. Tolosa, G. Kickelbick, V. Presser, Silicon oxycarbide beads from continuously produced polysilsesquioxane as stable anode material for lithium-ion batteries, ACS Appl. Energy Mater. 1 (2018) 2961–2970, https://doi.org/10.1021/acsaem.8b00716.
[9] G.D. Sorarù, G. D'Andrea, R. Campostrini, F. Babonneau, G. Mariotto, Structural characterization and high-temperature behavior of silicon oxycarbide glasses prepared from sol-gel precursors containing Si-H bonds, J. Am. Ceram. Soc. 78 (1995) 379–387, https://doi.org/10.1111/j.1151-2916.1995.tb08811.
[10] S. Choi, D.S. Jung, J.W. Choi, Scalable fracture-free SiOC glass coating for robust silicon nanoparticle anodes in lithium secondary batteries, Nano Lett. 14 (2014) 7120–7125, https://doi.org/10.1021/nl503620z.
[11] Z. Wu, W. Lv, X. Cheng, J. Gao, Z. Qian, D. Tian, J. Li, W. He, C. Yang, A nanostructured Si/SiOC composite anode with volume-change-buffering microstructure for lithium-ion batteries, Chem. Eur J. 25 (2019) 2604–2609, https://doi.org/10.1002/chem.201805255.
[12] Y. Jiang, C. Li, R. Yu, Y. Wang, L. Zhou, Realizing sub-5 nm red phosphorus dispersion in a SiOx/C matrix for enhanced lithium storage, ACS Appl. Mater. Interfaces 14 (2022) 26775–26781, https://doi.org/10.1021/acsami.2c05293.
[13] H.C. Huang, B.C. Huang, H.P. Hsu, C.W. Lan, Synthesis of silicon oxycarbide beads from alkoxysilane as anode materials for lithium-ion batteries, ACS Omega 8 (4) (2023) 4165–4175, https://doi.org/10.1021/acsomega.2c07242.
[14] M. Weinberger, C. Pfeifer, S. Schindler, T. Diemant, R.J. Behm, M. Wohlfahrt-Mehrens, Submicron-sized silicon oxycarbide spheres as anodes for alkali ion batteries, J. Mater. Chem. A 3 (2015) 23707–23715, https://doi.org/10.1039/c5ta06277b.
[15] H. Shi, A. Yuan, J. Xu, Tailored synthesis of monodispersed nano/submicron porous silicon oxycarbide (SiOC) spheres with improved Li-storage performance as an anode material for Li-ion batteries, J. Power Sources 364 (2017) 288–298, https://doi.org/10.1016/j.jpowsour.2017.08.051.
[16] M. Wilamowska-Zawlocka, P. Puczkarski, Z. Grabowska, J. Kaspar, M. Graczyk-Zajac, R. Riedel, G.D. Sorarù, Silicon oxycarbide ceramics as anodes for lithium ion batteries: influence of carbon content on lithium storage capacity, RSC Adv. 6 (2016) 104597–104607, https://doi.org/10.1039/c6ra24539k.
[17] A.F. Demirörs, A. Van Blaaderen, A. Imhof, A general method to coat colloidal particles with titania, Langmuir 26 (2010) 9297–9303, https://doi.org/10.1021/la100188w.
[18] Z. Wu, X. Cheng, D. Tian, T. Gao, W. He, C. Yang, SiOC nanolayers directly-embedded in graphite as stable anode for high-rate lithium ion batteries, Chem. Eng. J. 375 (2019) 121997, https://doi.org/10.1016/j.cej.2019.121997.
[19] B. Dong, Y. Han, T. Wang, Z. Lei, Y. Chen, F. Wang, H. Abadikhah, S.A. Khan, L. Hao, X. Xu, R. Cao, L. Yin, S. Agathopoulos, Hard SiOC microbeads as a high-performance lithium-ion battery anode, ACS Appl. Energy Mater. 3 (2020) 10183–10191, https://doi.org/10.1021/acsaem.0c01910.
[20] X. Liu, K. Xie, J. Wang, C. Zheng, Y. Pan, Si/Si-O-C composite anode materials exhibiting good c rate performances prepared by a sol-gel method, J. Mater. Chem. 22 (2012) 19621–19624, https://doi.org/10.1039/c2jm34011a.
[21] S. Gong, Y. Lee, J. Choi, M. Lee, K.Y. Chung, H.G. Jung, S. Jeong, H.S. Kim, In situ mesopore formation in SiOx nanoparticles by chemically reinforced heterointerface and use of chemical prelithiation for highly reversible lithium-ion battery anode, Small 19 (2023) 1–14, https://doi.org/10.1002/smll.202206238.
[22] K. Xia, L. Qu, X. Liu, H. Han, Z. Hou, Y. Li, S. Deng, Effect of SnCl2 addition on the structure and lithium storage performance of SiOC anodes, Appl. Surf. Sci. 506 (2020) 144775, https://doi.org/10.1016/j.apsusc.2019.144775.
[23] R. Tian, J. Wang, Z. Xu, X. Guo, W. Lei, R. Ding, Y. Zhang, H. Yang, Constructing Bi-continuous macroporous SiOC as high-performance lithium-ion battery anode, J. Porous Mater. 30 (2023) 23–32, https://doi.org/10.1007/s10934-022-01319-w.
[24] X. Chen, S. Zhou, B. You, L. Wu, Mechanical properties and thermal stability of ambient-cured thick polysiloxane coatings prepared by a sol-gel process of organoalkoxysilanes, Prog. Org. Coating 74 (2012) 540–548, https://doi.org/10.1016/j.porgcoat.2012.01.021.
[25] X. Meng, H. Huo, Z. Cui, X. Guo, S. Dong, Influences of oxygen content on the electrochemical performance of a-SiOx thin-film anodes, Electrochim. Acta 283 (2018) 183–189, https://doi.org/10.1016/j.electacta.2018.06.095.
[26] M. Han, J. Yu, Pressure-induced vapor synthesis of carbon-encapsulated SiOx/C composite spheres with optimized composition for long-life, high-rate, and high-areal-capacity lithium-ion battery anodes, Energy Technol. 7 (2019) 1900084, https://doi.org/10.1002/ente.201900084.
[27] J. Kaspar, M. Graczyk-Zajac, R. Riedel, Carbon-rich SiOC anodes for lithium-ion batteries: part II. role of thermal cross-linking, Solid State Ionics 225 (2012) 527–531, https://doi.org/10.1016/j.ssi.2012.01.026.
[28] D. Knozowski, M. Graczyk-Zając, D. Vrankovic, G. Trykowski, M. Sawczak, D.M. De Carolis, M. Wilamowska-Zawłocka, New insights on lithium storage in silicon oxycarbide/carbon composites: impact of microstructure on electrochemical properties, Composites, Part B 225 (2021) 1–11, https://doi.org/10.1016/j.compositesb.2021.109302.
[29] F. Wang, S. Lin, X. Lu, R. Hong, H. Liu, Poly-dopamine carbon-coated stable silicon/graphene/CNT composite as anode for lithium ion batteries, Electrochim. Acta 404 (2022) 139708, https://doi.org/10.1016/j.electacta.2021.139708.